Article

Reconstructing the Last 71 ka Paleoclimate in Northeast China by Integrating Typical Loess Sections

Juan Li [1], Kristofor R. Brye [2], Zhong-Xiu Sun [1], Phillip R. Owens [3], Zhuo-Dong Jiang [1,*], Tian-Hao Wang [1], Meng-Ge Zhang [1] and Qiu-Bing Wang [1,*]

[1] College of Land and Environment, Shenyang Agricultural University, Shenyang 110866, China; lijuan20161095@163.com (J.L.); sun19871001@126.com (Z.-X.S.); wangtianhao@dlu.edu.cn (T.-H.W.); menggezhang@stu.syau.edu.cn (M.-G.Z.)

[2] Department of Crop, Soil, and Environmental Sciences, University of Arkansas, Fayetteville, AR 72701, USA; kbrye@uark.edu

[3] USDA-ARS Dale Bumpers Small Farms Research Center, Booneville, AR 72927, USA; phillip.owens@usda.gov

* Correspondence: zhuodongjiang@163.com (Z.-D.J.); qbwang@syau.edu.cn (Q.-B.W.)

Abstract: Long-term continuous deposits and well-preserved thick loess sections are natural archives for the reconstruction of global climate change. However, the loess sections are often discontinuous owing to soil erosions and accumulations. This study aimed at reconstructing long-term continuous paleoclimatic records by integrating the target sections of two typical loess sequences in northeast (NE) China. One section, the Dajiugang (DJG) section, was investigated and sampled, and the Sanbahuo (SBH) section was used as the target for integrating and reconstructing the paleoclimate. Sedimentary, pedogenesis, and luminescence dating analyses were conducted to analyze the potentials for reconstructing the paleoclimate by integrating two typical loess sections. The results indicated that the paleoclimate records derived from the DJG section can be used to reconstruct the continuous paleoclimate of NE China by integrating them with the SBH section. The paleoclimate information inferred from the DJG section could impute paleoclimate data from 71 to 11.7 ka, which were missing in the SBH section. The paleoclimate of NE China generally consisted of three periods from 71 to 11.7 ka: cold and dry from 29 to 11.7 ka, alternately cold and warm from 57 to 29 ka, and warm and wet to cold and dry from 71 to 57 ka. Integrating the target loess sections can contribute to reconstructing regional long-term continuous paleoclimate records where discontinuous loess sequences occurred.

Keywords: soil integrating; loess–paleosol section; paleoclimate reconstruction; pedogenesis

1. Introduction

Loess, deep-sea sediments, and polar ice cores are regarded as major natural archives of global climate change records [1,2]. Compared to deep-sea sediments and polar ice cores, loess is widely distributed and relatively easily accessible for analyses [3]. Analyses of loess in central China [4–6], the East European Plain [7–10], mid-continental north America [11], and the Mediterranean region [12] have led to considerable progress in reconstructing paleoclimates. The paleoclimate of China since 2.4 Ma had been reconstructed using loess deposits in the Loess Plateau. However, the long-term paleoclimate of other regions still remains poorly understood due to long-term paleoclimate records being difficult to obtain from natural sources in the environment [1,13,14].

The information obtained from loess in various regions supports a better understanding of the global climate [15,16]. A prerequisite for assessing paleoclimate change recorded in loess is that the deposits must be continuous [17]. The age of loess formation, the information preserved, and the paleoclimate reflected by the loess varied with regional environment conditions [18–20]. Therefore, paleoclimate projections from individual regions cannot be

directly applied to other regions with different environmental conditions [21]. The distribution and thickness of loess deposits from various geographic regions differ by regional material sources and the deposition environment [17,22–24]. During loess deposition, erosion and accumulation occurred simultaneously due to regional sedimentological factors, such as topography, geomorphology, internal and external geological forces [20]. Long-term continuous deposits and ideal loess sections are difficult to identify in nature because the lithology of loess strata varies greatly in diverse geomorphic areas [25]. Therefore, integrating similar sections from different sites or from different periods of deposition is a potentially useful technique for reconstructing a long-term continuous record of the paleoclimate of a region. The foundations of integration generally require at least two strategically selected sections with similar pedogenesis processes and parent materials. However, a simultaneous study of two or more sections is time consuming and labor intensive, and the layers between sections do not always correspond exactly. Reconstructing long-term continuous paleoclimate records by integrating the target loess sections from a region would increase efficiency. The prerequisite for integration is the determination of an ideal target section in a specific region. The ideal target section should be as thick as possible and contain as many strata deposited over the long term as possible, even if some layers at different ages in the target section are missing. Thus, more loess sections should be investigated, and the missing layers in the target sections should be integrated to form a long-term paleoclimate record.

Even northeast (NE) China borders the eastern edge of the Eurasian Loess Belt [24], which contains extensive thick loess deposits [26]. Long-term and continuous paleoclimatic records from loess deposits in NE China are scarce. Integrating the target section can be an alternative method for reconstructing the paleoclimate of NE China. Specifically, detailed data compilations, analyses of the loess sections in NE China, and a field survey have indicated that the Sanbahuo (SBH) section could be regarded as an ideal target section representing NE China. The thickness of the SBH section is 59.9 m, and the deposits date back to 1.22 Ma, which is the oldest known loess section discovered in NE China [27]. The SBH loess section has several strata containing paleoclimatic information, particularly in the lower part, and it has considerable potential for reconstructing the long-term paleoclimatic history of the region [27]. Yi et al. [28] concluded that the SBH section has preserved a relatively complete loess sequence since the late Early Pleistocene era, comprising the Malan (Late Pleistocene, L_1), the upper Lishi (Middle Pleistocene, S_1–L_5), and the lower Lishi (Middle Pleistocene, S_5–L_{15}) loess deposits. However, the upper part of the SBH section— at a depth of ~10 m—and the MS curve have not noticeably changed since 84 ka [27], indicating that the climate did not change during this period, which is contrary to the rapid climate fluctuations during the entirety of the last glacial period [21]. There was only one loose loess layer in the upper part (L_1–S_1 layer) of the SBH section, which was found during the field investigation. This might indicate that the upper part of the SBH section is incomplete and could affect the paleoclimate interpretation of the SBH section. To eliminate negative effects, the L_1 layer of the SBH section was excluded and integrated into another section to produce a continuous composite record from 1.22 Ma [27]. Thus, well-preserved loess sections, which can be integrated with the SBH section, need to be identified to reconstruct a long-term continuous paleoclimatic record.

The paleoclimate information has been interpreted based on loess properties, such as grain size [1,29–31] and magnetic susceptibility [32–35]. The paleoclimate signals recorded in loess might have been modified to varying degrees by post-depositional processes, such as pedogenesis, which is a weathering process, which occurs under relatively warm and humid conditions [17]. Soil properties are derived from the depositional environment and the pedogenic environment after wind-blown particles are deposited. The pedogenic process is induced by climate and parent materials [36] and is controlled by environmental factors over time [37]. During slow pedogenic processes, chemical weathering is controlled by a specific climate, which comprises mostly downward-moving processes, including eluviation and illuviation [38], especially of calcium carbonate and clays. Soil properties vary due to different depositional environments and soil pedogenic processes or the degree of soil development.

Therefore, loess strata with different properties can reflect climate change and the degree of soil development during loess depositional periods [20,24]. The information interpreted from the loess sequence is not only mixed but also has significant traces of the influence of regional climate environment. Thus, the climatic environment reflected by the loess indicators is initially regional. Based on this, deeper regional tests and global comparisons of multiple indicators can refine the information, which reliably reflects global climate change [21,39]. However, paleoclimatic information interpreted using loess properties is mainly derived from the China Loess Plateau (CLP), while paleoclimatic changes in NE China are rarely studied.

The prerequisites for integrating two sections are that they must be of the same sediment type, genesis process, depositional age, and geomorphic features. Therefore, this study aimed to determine the feasibility of reconstructing long-term continuous paleoclimate records by integrating the loess target sections from NE China. One typical loess section (DJG section) in NE China was sampled and integrated with the already known SBH loess section to overcome stratigraphic incompleteness and was used to reconstruct paleoclimate changes since 71 ka.

2. Materials and Methods

2.1. Study Area and Loess Sections

The study area—where the main landform comprises high elevation in the west and low elevation in the east—is situated in Chifeng, NE China. The region consists of hills and valleys with elevations ranging from 661 to 1384 m (Figure 1) [40]. The loess deposited in this area is mainly Quaternary Aeolian loess [24]. The area has a typical temperate continental monsoon climate influenced by East Asian Monsoon circulation dynamics, where the ranges of mean annual temperature (from 1951 to 2013) and precipitation are 0–7 °C and 300–500 mm, respectively [41].

The DJG loess section (42°18′4″ N, 118°38′34″ E) is exposed on a terrace, where the Yin and the Seliga Rivers meet. The DJG loess section is located in a gully about 2.4 km northwest from the SBH section (42°18′27″ N, 118°41′17″ E) (Figure 1c). The DJG section's lithology mainly consists of ten pedostratigraphies, including light brown loess layers ($L_{1-2}S_2$ and $L_{1-3}S_1$) interbedded with weakly developed paleosols ($L_{1-1}S$, $L_{1-2}S_1$, $L_{1-2}S_3$, and $L_{1-3}S_2$), red paleosol layers (S), and loess layers ($L_{1-1}L$, $L_{1-2}L$, $L_{1-3}L$) (Figure 2). According to the field guidelines by Schoeneberger et al. [42], the loess section consists of 20 genetic horizons within 12.32 m depth.
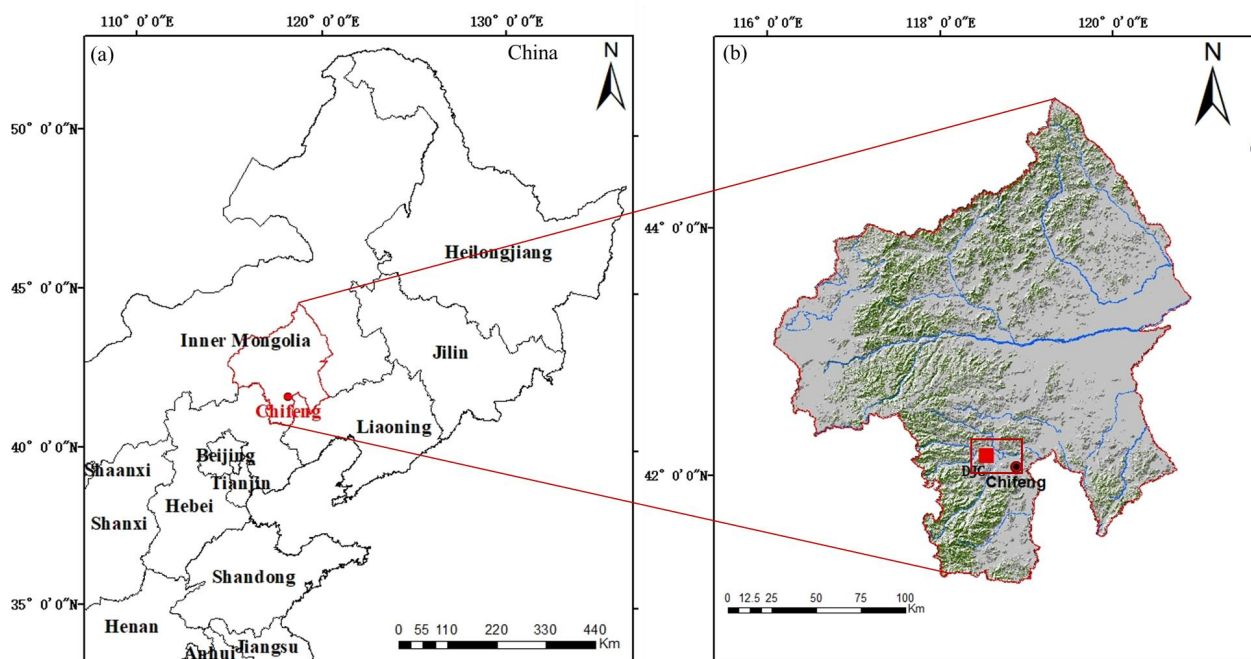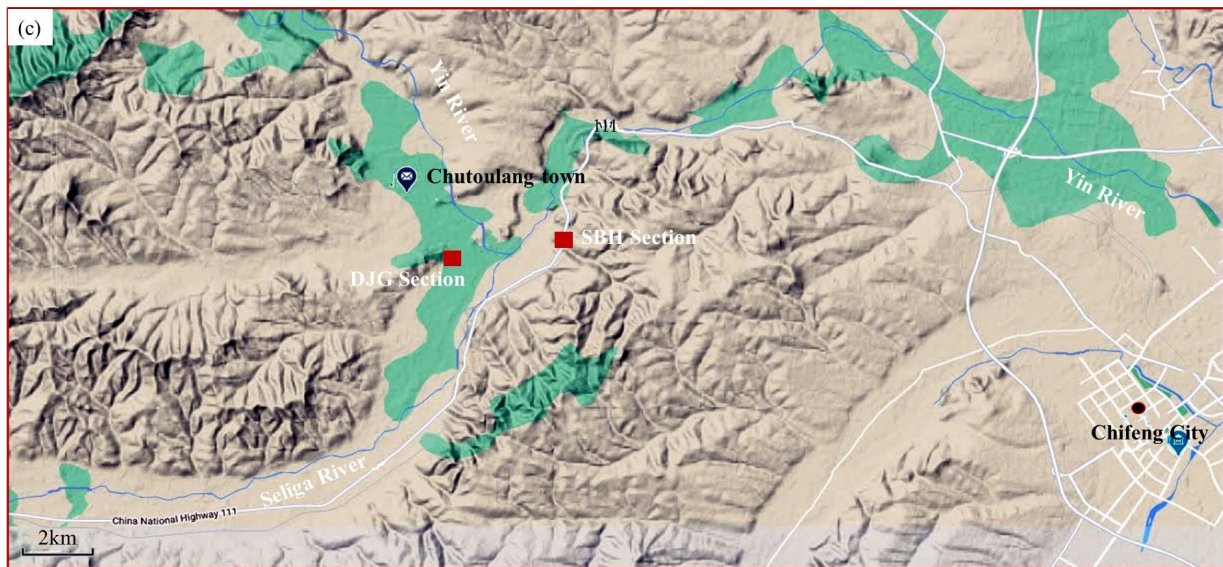

Figure 1. *Cont.*

Figure 1. Location map of the study area and sections. (**a**) The red square on the inset map shows the location of Chifeng in NE China, (**b**) the location of the investigated section in Chifeng, (**c**) landforms of the study region and locations of the investigated sections, and the red square represents the Dajiugang (DJG) loess section and the Sanbahuo (SBH) loess section, respectively.
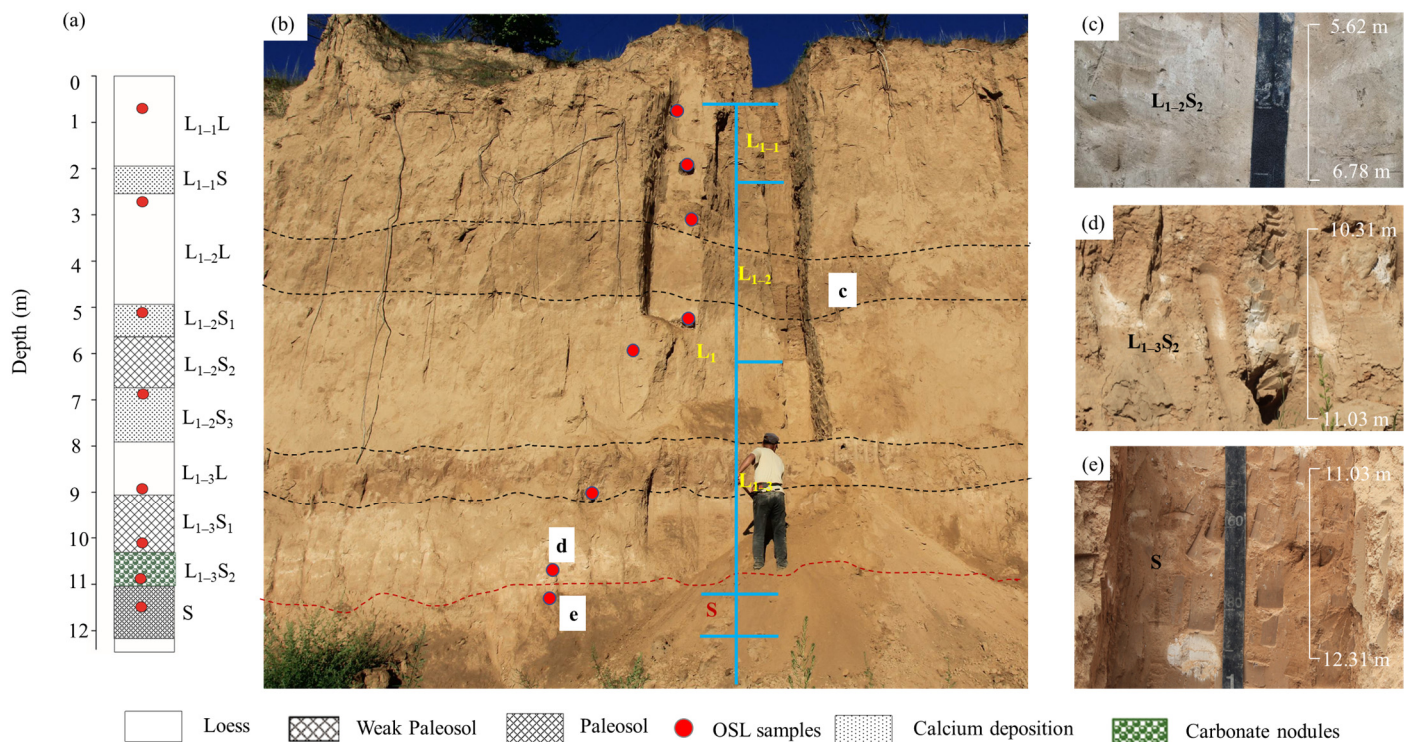
Figure 2. The sampled section. (**a**) Lithology of the DJG section; the solid red circles indicate the location of optically stimulated luminescence (OSL) samples. (**b**) The DJG section with pedostratigraphy indicated. (**c**) Part of the $L_{1-2}S_2$ layer of the DJG loess section. (**d**) Part of the $L_{1-3}S_2$ layer. (**e**) Part of the S layer of the DJG loess section.

2.2. Soil Sampling and Laboratory Analysis

Approximately 30 cm of the exposed soil surface was removed for describing the soil morphology characteristics (i.e., color, texture, structure, compactness, and horizons) and sampling [43–45]. Following the description, pedostratigraphies, genetic horizons,

and 5 cm interval soil samples were collected to ascertain various characteristics (i.e., soil age dating, chemical and physical properties, and magnetic susceptibility): (1) a total of 8 optically stimulated luminescence (OSL) samples were collected from the freshly exposed surface located at the pedostratigraphic boundaries using light-avoided steel cylinders with a diameter of 5 cm and a length of 20 cm [46]; (2) 20 genetic horizon samples were collected for physical and chemical analyses; (3) a total of 247 samples were collected at 5 cm intervals from the bottom to the top of the DJG section for measurement of magnetic susceptibility (MS) and grain-size distribution. All soil samples were transported to the laboratory, and the genetic horizon and 5 cm interval samples were air-dried for 7 days. The air-dried samples were cleared of roots and other organic debris. Subsequently, the soil was ground and passed through a 2 mm screen to prepare it for further laboratory analysis.

The MS2 meter was utilized to measure the low-frequency mass MS of 247 samples at a frequency of 470 Hz with an error rate of 1%. The measurements were normalized by mass [47]. Organic matter and carbonates within the soil matrix were removed using the 10% H_2O_2 and 10% HCl solution, respectively [48]. The grain size was determined using a Malvern 2000 laser diffractometer (Malvern Instruments Ltd., Malvern, UK) [49]. The soil pH was determined potentiometrically at a soil/solution ratio of 1:2.5 using a PHS-3C pH Meter [50]. Soil bulk density was determined by dividing the mass of soil matrix in the cylindrical core by the volume [51]. Soil carbonate concentrations were measured using the modified gas evolution method [52]. The major elemental composition was determined using inductively coupled plasma (ICP) [53].

2.3. OSL Soil Age Dating

2.3.1. Sample Preparation

The OSL samples enclosed in steel tubes were transported to the laboratory under sealed and light-protected conditions. The preprocessing of OSL samples aimed to extract the sedimentary quartz for measurement of the radiation dose and estimating the loess deposition time. The preprocessing steps were conducted in subdued red-light conditions (center wavelength: 655 ± 30 nm) in the laboratory. The unexposed soil samples were weighed around 100 g into the 1000 mL beaker and soaked with distilled water, and 30% H_2O_2 and 30% HCl were added to remove the organic matter and carbonates, respectively. Then, the soil suspensions were washed and filtered for neutralization with distilled water [54]. Afterward, the fine-sized mixed minerals (diameter: 4–11 μm) were separated from the suspensions according to Stokes' Law and soaked in fluosilicic acid for about 3 days to exclude feldspar-like minerals to purify fine-grained quartz. Lastly, the purified fine-grained quartz for further measurement can be homogeneously precipitated on stainless steel discs using ethanol [55,56].

After the fine-sized mixed minerals were separated, the residual samples were oven-dried at 40 °C and sieved to extract the coarse-sized mixed minerals with a diameter of 90–125 μm. The feldspar ($\rho < 2.62$ g/cm^3) and heavy minerals ($\rho > 2.66$ g/cm^3) within the coarse-sized mixed minerals were removed using polytungstate solutions. Then, the remaining mineral grains were soaked in a 40% HF solution for 1 h to remove the surface portion of the feldspar and quartz grains affected by α-rays. Later, the samples were soaked in 35% fluorosilicate for about 2–5 days and washed with warm HCl (10%) to remove the precipitated fluorides for purifying quartz grains (90–125 μm). Lastly, the purified quartz grains were fixed in the center area of the 9.7 mm diameter stainless steel discs using silicone oil to determine the equivalent dose (D_e) [57,58].

2.3.2. D_e and Dose Rate Determination

The OSL measurements were performed on a Risø TL/OSL-DA-20 reader [59], and the tests were controlled by the sequence (program) set by the computer. The D_e values of quartz (90–125 μm) were measured using the single-aliquot regenerative-dose (SAR) protocol (Table 1) [55,60]. Different doses produced different OSL signal intensities, which were corrected for susceptibility changes by the test dose. A dose growth curve was

established using the corrected OSL signal intensity for each irradiation dose. Then, the corrected natural OSL signal intensity was projected onto the growth curve, and the corresponding equivalent dose was calculated by backward extrapolation.

Table 1. Outline of dose measurement protocols used in this study. Single-aliquot regenerative-dose (SAR) protocol [60], simple multiple-aliquot regenerative-dose (SMAR) protocol [54,60].

Step	SAR Protocol	Observed [c]	SMAR Protocol	Observed [d]
1	Given dose, Di [a] (i = 0, 1, 2, 3...)	-	Natural dose	-
2	Preheat, (200~260 °C, 10 s)	-	Preheat (260 °C, 10 s)	-
3	IR stimulation [b] (125 °C, 60 s)	-	IR stimulation (125 °C, 60 s)	
4	Blue light stimulation (125 °C, 60 s)	L_x	Blue light stimulation (125 °C, 60 s)	L_i
5	Test dose	-	Test dose	
6	Cut heat (160 °C, 10 s)	-	Cut heat (220 °C, 10 s)	-
7	IR stimulation (125 °C, 60 s)	-	IR stimulation (125 °C, 60 s)	-
8	Blue light stimulation (125 °C, 60 s)	T_x	Blue light stimulation (125 °C, 60 s)	T_i
9	Return to step 1	-		

[a] For the natural sample, i = 0, and D_0 = 0 Gy. [b] The stimulation time is dependent on stimulation light intensity. [c] L_x and T_x are derived from the initial OSL signal (0.3 or 0.8 s) minus a background estimated from the last part of the stimulation curve. [d] The equivalent dose value is the ratio of natural dose to its post-test dose OSL signal (L_i/T_i).

The D_e values of purified quartz (4~11 μm) were measured using the simple multiple-aliquot regenerative-dose (SMAR) protocol (Table 1) [54,60]. At the end of the multi-aliquot natural- and regenerative-dose OSL signal (Li) test, all aliquots were irradiated with the measured dose for one hour, and the resulting sensitivity change was monitored and corrected with the measured dose OSL signal (Ti). The equivalent dose value is the ratio of the natural dose to post-test dose OSL signal (Li/Ti) [57].

For all samples, inductively coupled plasma mass spectrometry (ICP-MS) was used to measure the uranium (U) and thorium (Th) concentrations, and K content was determined by inductively coupled plasma optical emission spectrometry (ICP-OES) analysis [58]. The experiment was conducted at the Analysis and Testing Center of the Institute of Earth Environment, Chinese Academy of Sciences.

The environmental dose rates can be calculated using the following equation:

$$D = 0.04\, D_\alpha + D_\beta + D_\gamma + D_c \tag{1}$$

where D represents environmental dose rates; D_α, D_β, and D_γ represent the dose rates (Gy/a) from α, β, and γ radiation in the environment. The values of D_α, D_β, and D_γ were obtained by converting the U, Th, and K concentrations in the samples and correcting for water content [61]. D_c represents the dose rate from cosmic rays.

Following the D_e and dose rate determination, the ages of OSL samples from the DJG section can be calculated using the following equation:

$$A = D_e/D \tag{2}$$

where A represents the age (in ka); D_e represents the equivalent dose (in Gy); D represents the environmental dose rate (in Gy/ka).

2.4. Data Analyses

2.4.1. Parent Material Uniformity

Cremeens et al. [62] summarized a mathematical quantitative equation for the uniformity value of the parent material.

$$UV = \frac{[(si + vfs)/(s - vfs)]upper}{[(si + vfs)/(s - vfs)]adjacent\ lower} - 1.0 \tag{3}$$

where *si* represents the silt (2–50 μm) concentration (%); *vfs* represents the very fine sand (50–100 μm) concentration (%); and *s* represents the sand (50–2000 μm) concentration (%).

2.4.2. Chronology

Interpolation based on the magnetization model (Equation (3)) was used to reconstruct the paleoclimate [63].

$$T_m \;=\; T_0 + (T_1 - T_0)\left(\sum_{i\,=\,1}^{m} aisi\right)\left(\sum_{i\,=\,1}^{n} aisi\right)^{-1} \tag{4}$$

where T_m represents the age of a layer (*i*); T_0 and T_1 represent the ages of the two control points; *n* represents the total number of layers between the two age control points; *m* represents the total number of layers before the age of the requested layer; *ai* represents the thickness of a layer; *si* represents the mass magnetization value of a layer. T_0 and T_1 can be any point in the section, $T_1 > T_0$.

2.4.3. Soil Redness Rating

The redness rating (RR) values can be used to estimate pedogenic strength, which can be computed using Equation (4) [64–66].

$$RR = (K - H) \times C/V \tag{5}$$

where K is 12.5; C represents the chroma; V represents the value; and H is determined according to hue (i.e., 10YR = 10, 7.5YR = 7.5, 5YR = 5, 2.5YR = 2.5).

2.4.4. Soil Chemical Weathering Intensity Index

The elemental molar ratios widely used in loess research include the Chemical Index of Alteration (CIA) [67], K_2O/Na_2O ratio [68], SiO_2/Al_2O_3 ratio (Sa), Fe_2O_3/Al_2O_3 ratio [69], ba value, and Ki value, which were used in this study to quantify the weathering intensity of the DJG section. The measured molar CaO content was corrected for Ca in apatite using the available measured P_2O_5 content, and the CaO/Na_2O molar ratio was assumed to not be greater than that in the silicate material. When the remaining mole of CaO (corrected for apatite) was greater than Na_2O, mNa_2O was adopted. In contrast, when the remaining mole of CaO was less than that of Na_2O, $mCaO^*$ was used [14,69].

3. Results

3.1. Soil Morphological Characteristics of the DJG Section

The thickness of the DJG section was 12.32 m. It can be observed that the pedostratigraphy was clear, as shown in Figure 2. The whole section was divided into loess (L_1) (0–11.03 m) and red paleosol (11.03–12.32 m) (S). The L_1 layer was divided into the pedostratigraphic sub-layers L_{1-1} (0–2.53 m), L_{1-2} (2.53–7.90 m), and L_{1-3} (7.90–11.03 m), each marked with a specific symbol throughout the section (Figure 2a). According to the soil color and calcium carbonate presence (Table 2), the L_{1-1} layer was divided into $L_{1-1}L$ (0–1.95 m) and $L_{1-1}S$ (1.95–2.53 m); the L_{1-2} layer was divided into $L_{1-2}L$ (2.53–4.92 m), $L_{1-2}S_1$ (4.92–5.60 m), $L_{1-2}S_2$ (5.60–6.78 m), and $L_{1-2}S_3$ (6.78–7.90 m); and the L_{1-3} layer was divided into $L_{1-3}L$ (7.90–9.09 m), $L_{1-3}S_1$ (9.09–10.31 m), and $L_{1-3}S_2$ (10.31–11.03 m). Among the layers, the $L_{1-1}S$, $L_{1-2}S_1$, and $L_{1-2}S_3$ layers had different degrees of calcium carbonate accumulation; the $L_{1-3}S_2$ layer formed calcium carbonate nodules of different sizes. In addition, the $L_{1-2}S_2$ and $L_{1-3}S_1$ layers were brown (10YR 4/4), and the S layer was red (i.e., a paleosol layer).

Table 2. Soil morphological characteristics of the DJG section.

GS [a]	PS [a]	LS [a]	Horizon	Depth (m)	Munsell Color	Structure [b]	Texture [c]	Notes
L$_1$	L$_{1-1}$	L$_{1-1}$L (0–1.95)	Ah	0–0.12	10YR4/4	2, F, SBK	SL	Common plant roots.
			AB	0.12–0.41	10YR5/6	2, F, SBK	SL	
			Bw	0.41~0.82	10YR4/4	2, F, SBK	SIL	Few white pseudomycelium [d].
			Bk	0.82~1.95	10YR7/4	2, M, SBK	SIL	
		L$_{1-1}$S (1.95–2.53)	2Bkb	1.95~2.53	10YR7/4	2, M, ABK	SIL	Many CaCO$_3$ accumulated.
	L$_{1-2}$	L$_{1-2}$L (2.53–4.92)	3Bb1	2.53~3.53	10YR7/4	2, M, SBK	SIL	Few white pseudomycelium.
			3Bb2	3.53~3.95	10YR6/4	2, M, SBK	SIL	
			3Bb3	3.95~4.92	10YR6/4	2, M, SBK	SIL	
		L$_{1-2}$S$_1$ (4.92–5.60)	3Bkb1	4.92~5.60	10YR6/4	2, M, SBK	SIL	Many CaCO$_3$ accumulated.
		L$_{1-2}$S$_2$ (5.60–6.78)	3Bkb2	5.60~6.02	10YR4/6	2, M, SBK	SL	Few white pseudomycelium.
			3Bb4	6.02~6.78	10YR4/4	2, M, ABK	SL	
		L$_{1-2}$S$_3$ (6.78–7.90)	3Bkb3	6.78~7.90	10YR4/4	2, M, SBK	SL	Many CaCO$_3$ accumulated.
	L$_{1-3}$	L$_{1-3}$L (7.90–9.09)	4Bb1	7.90~8.34	10YR4/4	2, M, SBK	SL	Few CaCO$_3$ accumulated. Few Fe-Mn nodules.
			4Bb2	8.34~9.09	10YR7/4	2, M, SBK	SL	
		L$_{1-3}$S$_1$ (9.09–10.31)	4Bkb1	9.09~9.32	10YR4/4	2, M, ABK	SL	Pores significantly increased, 5% white pseudomycelium, few CaCO$_3$ accumulated.
			4Bkb2	9.32~10.31	10YR4/6	2, M, ABK	SL	
		L$_{1-3}$S$_2$ (10.31–11.03)	4Bkb3	10.31~11.03	10YR6/6	2, M, ABK	SIL	30% CaCO$_3$ nodules (6–20 mm; the thickest part of the carbonate nodules can reach 54 cm) reacted strongly to dilute acid.
S	S	S (11.03–12.32)	5Btrb1	11.03~11.81	5YR5/6	2, M, ABK	SIL	3% Fe-Mn nodules, 2% clay films, few CaCO$_3$ nodules, reacted strongly to dilute acid.
			5Btrb2	11.81~12.13	5YR5/4	2, M, ABK	SIL	
			5Btrb3	12.13~12.32	5YR4/6	2, M, ABK	SIL	

[a] GS, geological strata; PS, pedostratigraphy; LS, layer symbol. [b] Soil structure: Grade: 1 = weak; 2 = moderate; 3 = strong; Size: F = fine; M = medium; Type: ABK = angular blocky; SBK = sub-angular blocky. [c] Soil texture: SL, sandy loam; SIL, silt loam. [d] Pseudomycelium = carbonate filaments.

3.2. Sedimentary Characteristics and Age of the DJG Section

3.2.1. Soil Age of the DJG Section

Depositional age determination of the DJG section was conducted at the Analysis and Testing Center of the Institute of Earth Environment, Chinese Academy of Sciences (Table 3). The D_e values range from 71.14 ± 2.65 Gy to 721.95 ± 15.48 Gy from the upper layer to the sub-layer. Correspondingly, the soil age of the upper layer is 17.94 ± 1.14 ka, and the soil age of the sub-layer is 196.34 ± 10.89 ka. The depositional ages of upper $L_{1-1}L$ (0.6 m), upper $L_{1-2}L$ (2.76 m), upper $L_{1-2}S_1$ (5.05 m), upper $L_{1-2}S_3$ (6.63 m), lower $L_{1-3}L$ (9.0 m), lower $L_{1-3}S_1$ (10.31 m), lower $L_{1-3}S_2$ (11.03 m), and middle S (11.31 m) were 17.94 ± 2.65, 34.27 ± 2.50, 39.27 ± 2.79, 41.67 ± 1.61, 66.97 ± 4.72, 71.50 ± 4.36, 181.58 ± 10.42, and 196.34 ± 10.89 ka, respectively (Table 3). The age of sample 6—collected at a depth of 10.31 m from the bottom of the $L_{1-3}S_1$ layer—was 71.5 ± 4.36 ka ($D_e = 277.26 \pm 4.92$ Gy), which was in agreement with the age (71 ka) of L_1/S_1 boundary within the margin of error [4]. Several papers had suggested that a reliable quartz OSL D_e value for loess distributed in China is around ~230 Gy (or lower than 300 Gy) and that the saturation age is around ~100 ka [9,57,58]. Two quartz samples—$L_{1-3}S_2$ and middle S—have D_e values higher than 300 Gy. The reliability of these two layers could not be confirmed in this study; therefore, all layers above the $L_{1-3}S_2$ layer (depositional age at 71.5 ± 4.36 ka) were studied. The ages of all samples, except those from the $L_{1-3}S_2$ and S layers, were close to expected values. The chronology of the DJG section was generated via linear interpolation of the MS model (Equation (4)).

Table 3. Environmental radioactivity and dating results.

| Sample ID	Depth (m)	U (ug/g)	Th (ug/g)	K (%)	Water Content (%)	Dose Rate [a] (Gy/ka)	OSL D_e [b] (Gy)	OSL Age (ka)
1	0.61–0.66	2.19 ± 0.08	10.10 ± 0.44	2.07 ± 0.05	8 ± 4	3.97 ± 0.21	71.14 ± 2.65	17.94 ± 1.14
2	2.76–2.81	2.56 ± 0.13	10.58 ± 0.45	2.03 ± 0.07	8 ± 4	4.02 ± 0.22	137.14 ± 6.61	34.15 ± 2.50
3	5.05–5.10	2.53 ± 0.06	10.42 ± 0.19	2.02 ± 0.05	9 ± 4	3.92 ± 0.21	153.89 ± 7.16	39.27 ± 2.79
4	6.63–6.68	2.95 ± 0.07	9.89 ± 0.16	2.00 ± 0.05	10 ± 5	3.29 ± 0.12	137.09 ± 2.24	41.67 ± 1.61
5	9.00–9.05	2.95 ± 0.08	12.30 ± 0.26	1.92 ± 0.07	10 ± 5	4.08 ± 0.24	273.12 ± 10.31	66.97 ± 4.72
6	10.31–10.36	2.85 ± 0.05	12.02 ± 0.20	1.83 ± 0.01	11 ± 5	3.88 ± 0.23	277.26 ± 4.92	71.50 ± 4.36
7	11.03–11.08	2.76 ± 0.07	11.28 ± 0.14	2.03 ± 0.01	14 ± 5	3.84 ± 0.21	697.62 ± 10.34	181.58 ± 10.42
8	11.31–11.36	2.19 ± 0.04	10.34 ± 0.11	2.30 ± 0.03	18 ± 5	3.68 ± 0.19	721.95 ± 15.48	196.34 ± 10.89

[a] The alpha efficiency for quartz was taken as 0.035 ± 0.003 [56]. [b] D_e is the equivalent dose.

3.2.2. Grain-Size Characteristics

The frequency curve of the DJG section showed a bi-modal distribution (Figure 3a), with the greatest peak at 30–70 μm—accounting for ~55% of the soil by weight relative to the basic dust fraction [20]—and a low peak at 5–10 μm. The ratio (%) reached a maximum mode size and decreased in both coarse and fine directions, with a long tail on the fine side, which was skewed toward the coarser side and was thus asymmetric. The cumulative curve of the DJG section (Figure 3b) was S-shaped, with straight line as the main body, and the samples comprised a coarse component (30–80%) with a modal size range of 35–43 μm. The cumulative curve of the DJG section contained inflection points at 3 and 9 Φ.

Considering the particle-size distribution of the DJG sections (Figure 4), the clay, silt, and sand fractions varied with depth and were mainly related to pedogenesis processes and the original deposition of eolian loess, as reported in a previous work [39]. The clay concentration in the L_{1-1} layer was <1%, and the silt (50–2 μm particle size) concentration increased to a maximum of 70% in the $L_{1-1}S$ layer; conversely, the sand concentration decreased to 29%, with little change in standard deviation (SD) in the vertical direction (Figure 4). The clay concentration in the L_{1-2} layer was <1%; the silt concentration decreased to a minimum of 29% in the $L_{1-2}S_3$ layer; meanwhile, the sand concentration reached 70%, with little change in SD. The clay concentration in the L_{1-3} layer first increased to 4% with depth in the $L_{1-3}S_1$ layer, then decreased to 1% in the $L_{1-3}S_2$ layer. The silt concentration gradually increased from 27% in the $L_{1-3}L$ layer to about 50% in the $L_{1-3}S_1$ layer. The sand

concentration gradually decreased from 70% in the $L_{1-3}L$ layer to about 50% in the $L_{1-3}S_1$ layer. The SD at the interface of the $L_{1-3}S_1$ and $L_{1-3}S_2$ layers sharply increased to 2.0, and the SD of the $L_{1-3}S_2$ layer was 1.4. The clay concentration in the S layer was 2%, and the silt concentration was ~70%, with a stable SD of 1.4. The distribution of individual silt fractions on a clay-free basis was 28% for silt particles of 50–2 μm in the $L_{1-2}S_3$ and $L_{1-3}L$ layers and up to 70% for the sand (≥50 μm) concentration in the $L_{1-2}S_3$ and $L_{1-3}L$ layers, which was numerically greater than in all other layers. Apart from the $L_{1-2}S_3$ and $L_{1-3}L$ layers, the concentration of silt particles (50–2 μm) was up to 60% in the remaining horizons, and the coefficient of variation (CV) of the silt concentration was 24 (Table 4). This suggested that the DJG loess section had a uniform source or parent material and a stable depositional environment. The coarse silt (CSI)/medium silt (MSI) ratios of the DJG section ranged from 3 to 6 with a CV of 17 (Table 4).
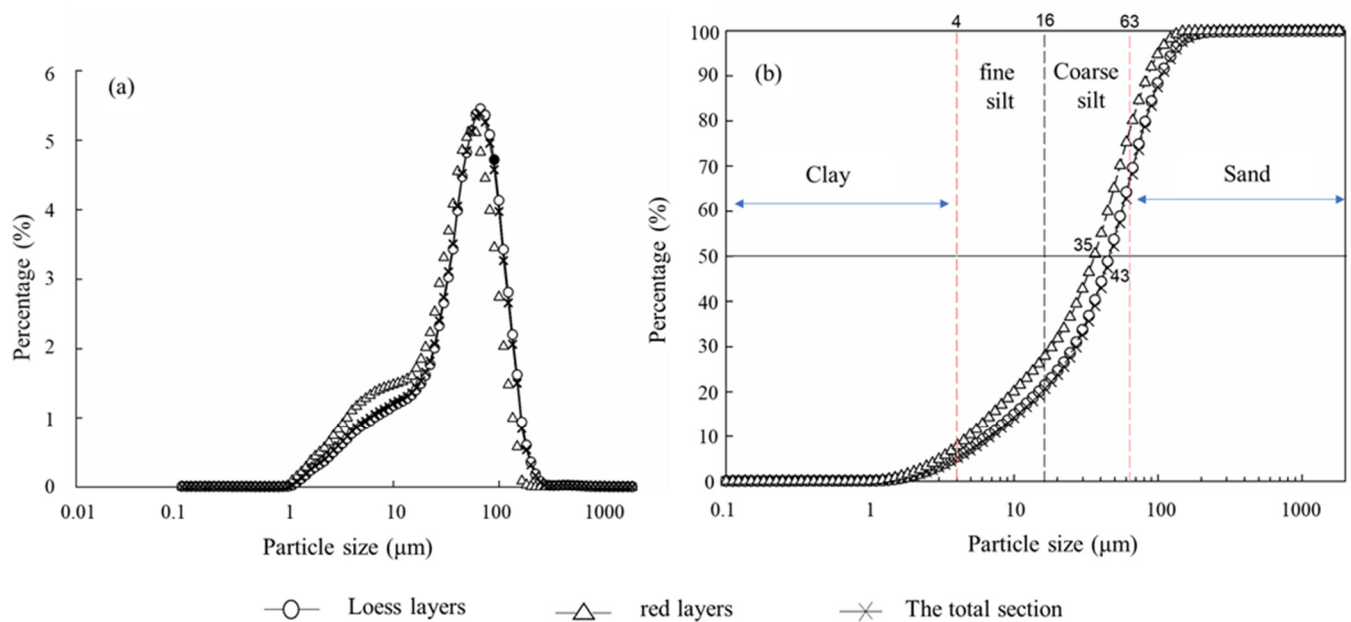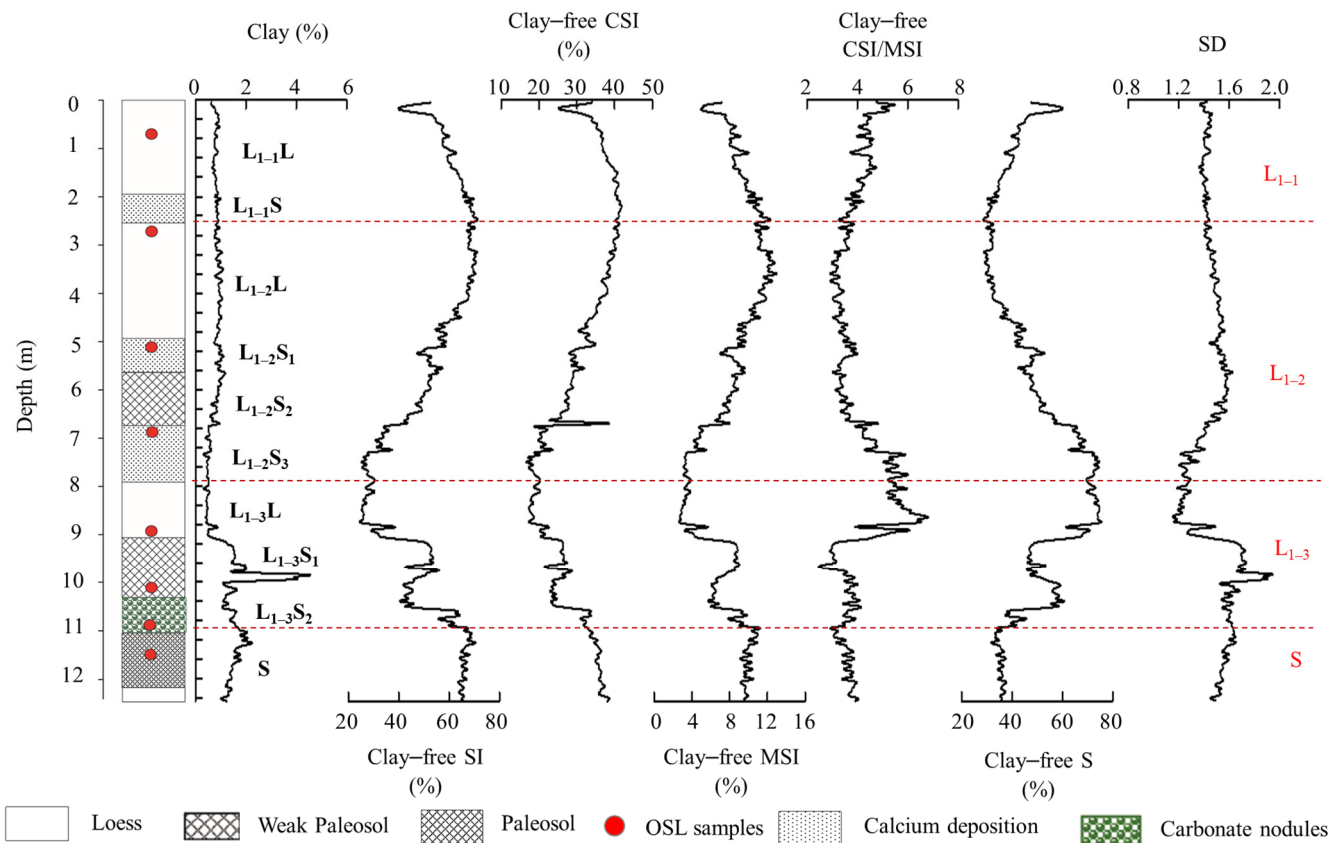

Figure 3. Grain-size distribution curve of the DJG loess section. (**a**) The grain-size frequency curve; (**b**) the grain-size cumulative curve.

Table 4. Clay-free grain-size distributions and UV and Ti/Zr ratio of the DJG section.

PS [a]	Depth (m)	SI [b] (%)	CSI/MSI [c]	VFS [d] (%)	S [e] (%)	UV	Ti (mg kg^{-1})	Zr (mg kg^{-1})	Ti/Zr
$L_{1-1}L$	0–1.95	58.3	4.4	34.7	41.7	0.06	3146	336	9.5
$L_{1-1}S$	1.95–2.53	68.9	3.7	27.7	31.1	0.11	3318	296	11.2
$L_{1-2}L$	2.53–4.92	66.0	3.3	28.3	33.9	0.09	3536	300	11.8
$L_{1-2}S_1$	4.92–5.62	53.6	3.6	34.5	46.4	0.12	3331	362	9.2
$L_{1-2}S_2$	5.62–6.78	48.4	3.5	36.0	51.6	0.05	3752	423	9.0
$L_{1-2}S_3$	6.78–7.90	30.2	5.0	45.6	69.8	0.10	3568	455	7.8
$L_{1-3}L$	7.90–9.09	28.8	5.6	47.8	71.2	0.07	3178	454	7.3
$L_{1-3}S_1$	9.09–10.31	48.9	3.3	34.9	51.1	0.08	3476	335	10.3
$L_{1-3}S_2$	10.31–11.03	56.8	3.6	33.4	44.7	0.23	3286	309	10.6
S	11.03–12.32	66.1	3.6	30.2	35.5	0.08	3960	36	12.2
	mean	53.8	4.0	34.9	46.6		3424	350	10.1
	SD [f]	13.2	0.7	6.2	13.0		253.3	63.3	1.6
	CV [g] (%)	24.6	17.6	17.7	27.9		7.4	18.1	15.8

[a] PS = pedostratigraphy; [b] SI = silt (2–50 μm); [d][c] CSI/MSI = coarse silt (50–20 μm)/medium silt (20–10 μm); [d] VFS = very fine sand (50–100 μm); [e] S = sand (50–2000 μm); [f] SD = standard deviation; [g] CV = coefficient of variation.

Figure 4. Variation in grain-size distribution of the DJG section with depth. SI (silt) = 50–2 μm particles; CSI (coarse silt) = 50–20 μm silt separate; MSI (medium silt) = 20–10 μm silt separate; and S (sand) = ≥50 μm sand particles.

3.2.3. Parent Material Uniformity of the DJG Section

The UV parameter (Equation (3)) and Ti/Zr ratio indicated uniformity of the sediment source [62,70]. Chen [71] reported that the UV tends to be 0, and the similarity of a parent material source is greater in two layers when the absolute UV is >0.6, indicating different parent materials in adjacent layers. The UVs of the DJG section were <0.6 in each layer (Table 4), indicating that the parent materials were uniform. Drees and Wilding [68] reported that a CV of the Ti/Zr ratio > 22% indicates non-uniform parent materials. In contrast, Chapman and Horn [72] reported that differences > 100% were required to detect lithologic changes. A CV of 15.82% for the Ti/Zr ratio suggested uniform materials throughout the DJG section. These results indicated that the parent material in the DJG section was uniform.

3.3. Soil Pedogenesis Characteristics

Soil bulk density, pH, $CaCO_3$ concentration, RR value, and weathering index changed with depth for the DJG loess section (Figure 5). The bulk density and $CaCO_3$ concentration in the L_{1-1} layer were ~1.4 g/cm^3 and 8%, respectively. The RR value (Equation (5)) and soil organic carbon (SOC) concentration in the L_{1-1} layer were ~2 and 10 g/kg, respectively. Soil pH increased with depth and ranged from 6.8 to 7.2. The MS was ~50 (10^{-8} m^3/kg). The K_2O/Na_2O and Fe_2O_3/Al_2O_3 ratios were 0.8 and 0.18, respectively. The CIA value was 49 in the lower part of the $L_{1-1}L$ layer and 52 in the $L_{1-1}S$ layer. The $(Al_2O_3 + Fe_2O_3)/(CaO + MgO + Na_2O)$ value (Ki) increased numerically with depth, and the $L_{1-1}S$ layer had a large Ki value due to calcium accumulation. The SiO_2/Al_2O_3 ratio (Sa) and $(CaO + K_2O + Na_2O + MgO)/Al_2O_3$ (ba) values gradually decreased numerically with depth, and the Sa and ba values were lowest in the $L_{1-1}S$ layer.
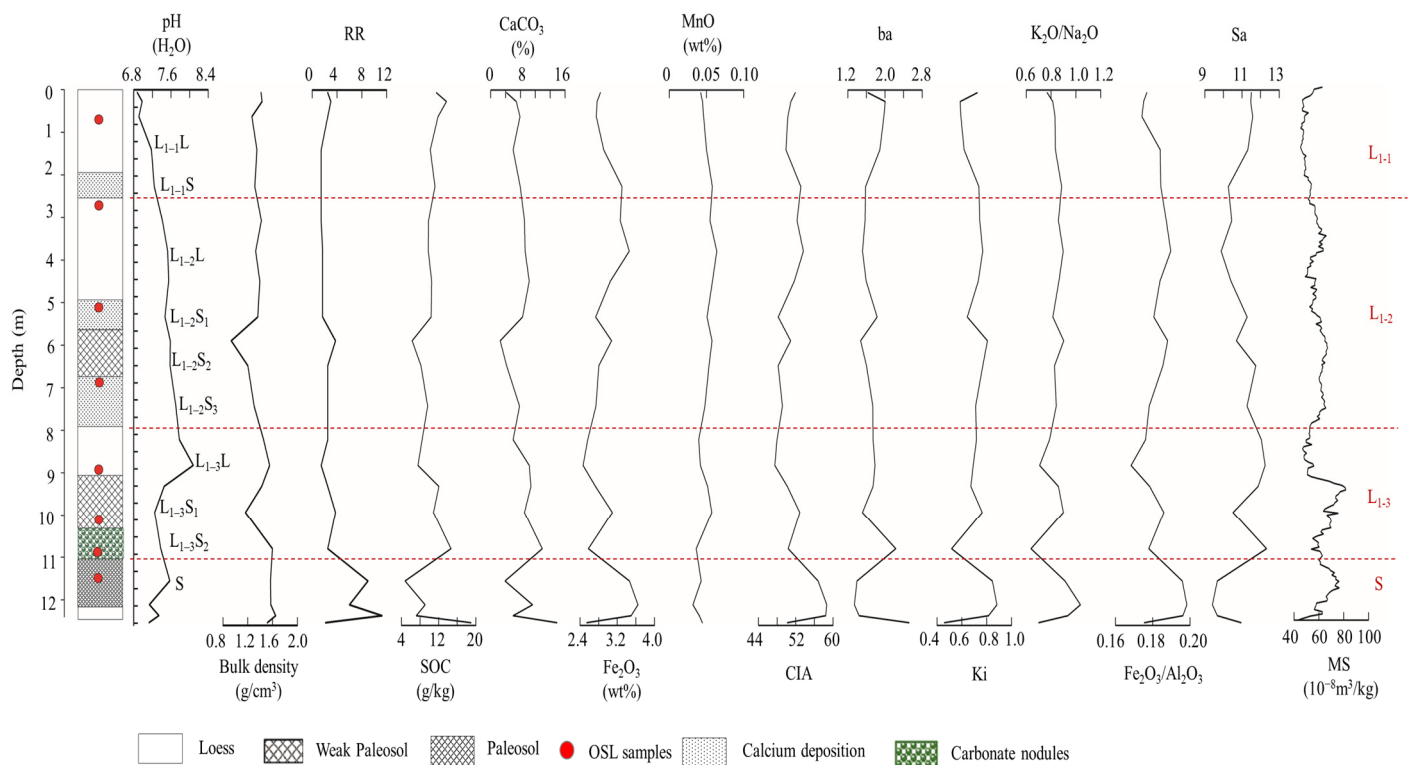
Figure 5. Change in soil pH, RR, bulk density, soil organic carbon (SOC), CaCO$_3$ (%), Fe$_2$O$_3$ (wt%), MnO (wt%), and weathering indices with depth for the DJG loess section.

Soil bulk density of the L$_{1-2}$ layer was a minimum of 0.81 g/cm^3 in the L$_{1-2}$S$_2$ layer and remained at ~1.4 g/cm^3 in the remaining layers. The SOC and CaCO$_3$ concentrations were low in the L$_{1-2}$S$_2$ layer—6 g/kg and 2%, respectively—with little variation in the other layers. Soil pH increased from 7.4 to 7.8 with depth. The RR value and Fe$_2$O$_3$ and MnO concentrations in the L$_{1-2}$S$_2$ layer increased with depth—4, 3.0 wt%, 0.05 wt%, respectively—compared to the adjacent layer (L$_{1-2}$S$_1$ and L$_{1-2}$S$_3$ layers). The Fe$_2$O$_3$ concentration was maximum in the L$_{1-2}$L layer (3.4 wt%), whereas the Sa ratio had a nadir of 9.5, which corresponded to the peak in the MS curve. The CIA and Ki values, as well as the K$_2$O/Na$_2$O and Fe$_2$O$_3$/Al$_2$O$_3$ ratios, were 52, 0.6, 0.9, and 0.19, respectively, whereas the ba and Sa ratios were 2 and 11, respectively, in the L$_{1-2}$S$_2$ layer.

Soil bulk density in the L$_{1-3}$L, L$_{1-3}$S$_1$, and L$_{1-3}$S$_2$ layers was 1.5, 1.2, and 1.6 g/cm^3, respectively. Soil pH in the L$_{1-3}$L layer reached maximum at 8.0, and it was 7.2 in all other layers. The RR value and Fe$_2$O$_3$ and MnO concentrations in the L$_{1-3}$S$_1$ layer were 4, 3.2, and 0.05 wt%, respectively. The SOC and CaCO$_3$ concentrations in the L$_{1-3}$S$_1$ layer were 11 g/kg and 8%, respectively. The CIA and Ki values, as well as the K$_2$O/Na$_2$O and Fe$_2$O$_3$/Al$_2$O$_3$ ratios in the L$_{1-3}$S$_1$ layer were 54, 0.8, 0.9, and 0.19, respectively, indicating a sharp increase corresponding to the peaks in the MS curve. The ba and Sa ratios were 1.4 and 10, respectively.

Soil bulk density in the S layer was 1.6 g/cm^3, and soil pH decreased from 7.4 to 6.9 with depth. The RR value and Fe$_2$O$_3$ concentrations ranged from 8 to 12 and from 3.2 to 3.6 wt%, respectively. The SOC and CaCO$_3$ concentrations were ~6 g/kg and ~4%, respectively. The S layer had the largest CIA and Ki values—as well as K$_2$O/Na$_2$O and Fe$_2$O$_3$/Al$_2$O$_3$ ratios—and the lowest ba and Sa ratios compared to the upper L$_1$ layer in the DJG loess section.

4. Discussion

4.1. Integrating a Typical Loess Section in NE China

4.1.1. Feasibility of Integrating Typical Sections

Full comparison of the sediment types, genesis processes, deposition ages, and geomorphic features of DJG and SBH sections is a prerequisite for integration. The DJG and SBH sections were derived from aeolian loess, which indicated the feasibility of integrating these two sections for paleoclimate reconstruction [27,41]. This inference was reasonable, given the bi-modal distribution of the frequency curve of grain-size distribution in the DJG section (Figure 3a). Bi-modal distribution is consistent with the loess found on the Loess Plateau in China [73], which also has a bi-modal distribution with overlapping coarse and fine grains—the main component of coarser grains. It has pronounced kurtosis and good sorting, which varies depending on the ratios of the two components and mode size. Furthermore, the greatest peak domain of the 30–70 μm coarse particles—accounting for ~55% of the soil by weight—indicated typical loess, and thus, an eolian origin [73]. The eolian particle dynamics indicated that the coarse-grain fraction was generally transported by surface winds over a short distance [74]. The cumulative curve of the grain-size distribution (Figure 3b) was S-shaped, with straight line as the main body of the curve, and contained 3 and 9 Φ inflection points. The size of grains transported in low-altitude suspended dust is >4–6 Φ or 4.3 Φ, whereas those <4.3 Φ on the ground are transported by being rolled or bounced (i.e., saltation) [75,76]. These results support the conclusion that the DJG section contained typical aeolian loess and that the transport mode of the DJG section was mainly low-altitude suspension, with a small portion of particles being transported by saltation.

A comparison of MS curve variations between the two loess sections indicated that the L_1 layer of the SBH section had no shifts with depth, whereas the DJG section varied with depth (Figure 6). The MS curve of the loess sequence reflects multi-cycle variations in the paleoclimate and can be compared with marine oxygen isotope records [4,77], further indicating that the DJG section contains multiple alternating cold–dry and warm–wet stages due to differences in pedogenesis [78]. A comparison of the color, geochemical indices, and soil weathering index variability provided additional support for the DJG section having undergone different pedogenic intensities.

Soil color is the most visual representation of soil properties, and changes in loess soil color are caused by local climatic conditions, strong or weak weathering and pedogenesis, and corresponding changes in the original composition [22,66]. The RR value represents the reddening process of the soil during pedogenesis and closely correlates with large and small lithostratigraphic values in paleosols and loess units, respectively [65]. The RR value of the $L_{1-2}S_2$, $L_{1-3}S_1$, and S layers was large in the DJG section, implying stronger pedogenesis than in the adjacent layers (Figure 5). The low calcium carbonate concentration in the $L_{1-2}S_2$, $L_{1-3}S_1$, and S layers indicated that decalcification had occurred. Geochemical indices indicated initial weathering and pedogenesis [79]. The degree of weathering was identified in the DJG section using the soil weathering index (Figure 5). The CIA can indicate pedogenesis and weathering. Fedo et al. [80] classified the degree of soil weathering based on CIA values of 50–60, 60–80, and >80 as primary, intermediate, and extreme, respectively. The CIA values of the L_1 layer were <55 (Figure 5), indicating that the layer was likely unweathered. The $L_{1-3}L$ layer had the lowest CIA value, indicating the weakest weathering in the entire section. The S layer had a CIA value of 60, indicating a primary degree of weathering. The CIA values of the $L_{1-2}S_2$, $L_{1-3}S_1$, and S layers were larger compared to the adjacent layers in the DJG section, implying a higher degree of soil weathering than in the adjacent layers.
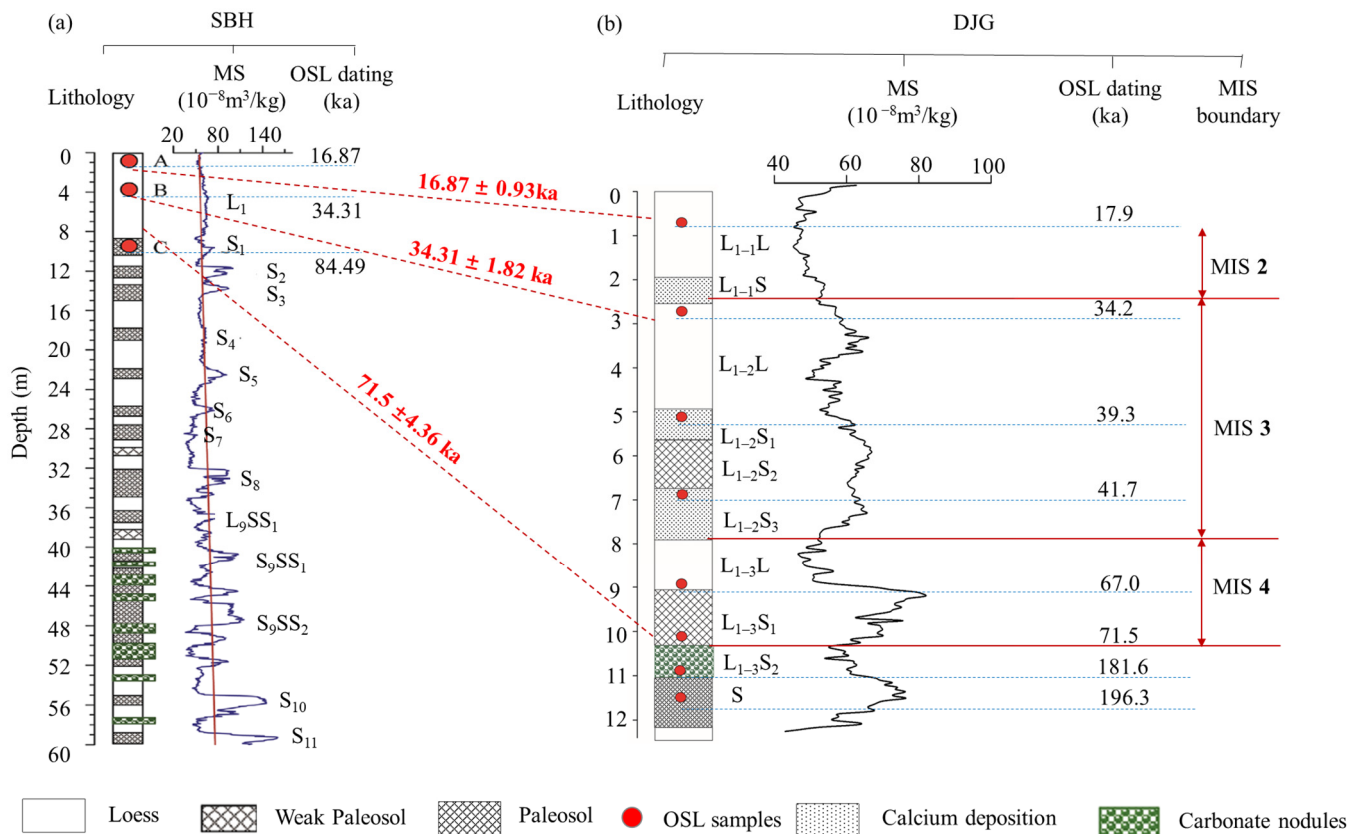
Figure 6. Comparison of the lithology, magnetic susceptibility (MS), and deposition age of the DJG loess section (**b**) with the SBH loess section (**a**) in NE China. The red dotted lines indicate the isochrons of the DJG section and the SBH section. The red lines indicate the boundaries of marine oxygen isotope stages (MIS). The blue dotted lines indicate the OSL age.

Because a relatively large carbonate concentration might impact the absolute chemical composition of loess owing to various degrees of leaching and illuviation during soil formation, element ratios are used to minimize the effect of carbonate dilution and infer past climate variation [81]. Liu [20] proposed that the Sa ratio gradually decreases with increased soil weathering, whereas the K_2O/Na_2O ratio tends to increase during soil formation. The Sa and K_2O/Na_2O ratios gradually decreased and increased, respectively, in the $L_{1-2}S_2$, $L_{1-3}S_1$, and S layers (Figure 5) due to different weathering intensities of soil formation. Li et al. [82] proposed that the ba value could reflect the leaching and migration of elements Ca and Na, whereas the Ki values could reflect the relative enrichment of Fe and Al. The large Ki values—as well as K_2O/Na_2O and Fe_2O_3/Al_2O_3 ratios—in the $L_{1-2}S_2$, $L_{1-3}S_1$, and S layers and the low ba values indicated enrichment of Fe and Al and leached Ca and Na due to strong weathering. The $L_{1-2}S_2$, $L_{1-3}S_1$, and S layers of the DJG section had numerically greater RR values, leached Ca and Na, and enriched Fe and Al caused by stronger pedogenesis compared to the L_1 layer in the SBH section. Thus, the DJG section had undergone different pedogenic intensities and recorded multi-cycle variations in the paleoclimate. Consequently, the DJG section can be integrated with the upper part (i.e., the L_1 layer) of the SBH section to overcome the missing paleoclimatic information in the SBH section.

4.1.2. Outcome of Integrating Two Typical Loess Sections

The lithostratigraphic comparison in the field and the depositional ages of the two sections showed that the L_1 layer of the DJG section (i.e., 10.31 m, 71.5 ka) could be integrated with the upper part (i.e., the L_1 layer) of the SBH section (Figure 6). The

isochrons between the two sections were established based on the reliable independent chronology of these two sections (Figure 6) [83].

The upper part of the $L_{1-3}S_1$ layer (10.31 m) was selected for integration because the $L_{1-3}S_1$ layer has continuous deposition, whereas the lower $L_{1-3}S_1$ layer has intermittent deposition. The deposited ages of the $L_{1-3}S_1$ and $L_{1-3}S_2$ layers were ~71.5 and ~181.58 ka, respectively. The deposited age of the $L_{1-3}S_2$ layer (i.e., with carbonate nodules) ranged from 181 ± 10.42 to 71.5 ± 4.36 ka. Depositional interruptions might be caused by erosion between depositional events, as one layer does not reflect climate changes over hundreds of thousands of years [84].

The SD of all particles in the DJG section provided additional support for the loess deposit being discontinuous, where the SD is often used to indicate uniformity of the sediment and distinguish the sedimentary environment [85,86]. Based on the large fluctuations in the SD of all particle sizes in the L_{1-3} layer of the DJG section, the DJG section was considered interrupted in the lower part of the L_{1-3} layer. This inference was reasonable, given that the SD was minimal in the upper part of the L_{1-3} layer (SD = 1.2), indicating good sorting. However, the SD sharply increased to 2.0 at the interface of the $L_{1-3}S_1$ and $L_{1-3}S_2$ layers, indicating poor sorting (Figure 4). The field investigation revealed a fine sand and gravel layer at the interface of the $L_{1-3}S_1$ and $L_{1-3}S_2$ layers, which might have been influenced by flowing water. Therefore, the interface of $L_{1-3}S_1$ and $L_{1-3}S_2$ layers might have experienced intermittent deposition. Moreover, the soil age in the lower part of the $L_{1-3}S_1$ layer was 71.5 ka; hence, the deposition was continuous until 71.5 ka and intermittent after 71.5 ka. The upper part of the $L_{1-3}S_1$ layer (10.31 m) was selected for integration with the SBH section deposited 71 ka ago. As the deposition of the DJG section was discontinuous during 84 ka–71 ka, another section should be integrated with the SBH section, so that a continuous record can be obtained from 1.22 Ma. However, the deposition of the DJG section has been continuous since 71 ka and intermittent after 71 ka; hence, 71 ka was selected for paleoclimate reconstruction and interpretation.

4.1.3. The Advantages and Limitations of Integrating the Loess Sections

Integrating the target sections of loess could reconstruct regional long-term continuous paleoclimate records where discontinuous loess sequences occurred. In addition, integrating the target sections of a region would render the study more purposeful and save a great amount of time and labor. Based on the integrated loess section, paleoclimate records can be rapidly and accurately reconstructed using soil age dating methods. However, a full comparison of the sediments, genesis processes, and geomorphologies of these sections is needed before integration, which requires detailed investigations and data as supports. The problem of homogeneity arises during the integration of sections. For example, the integration parts of the two sections may have the same depositional age but different genesis. The integration part may have the same depositional age, but the parent material may not be uniform. The depositional ages, genesis processes, parent materials must be the same for the junction layers of the integration sections, which are very difficult to find. These integration prerequisites restrict the wide use of integration. Another problem is that sampled sections may also experience depositional discontinuity events, and only the depositional continuum layer would be integrated with the target section. The discontinuous depositional layer of the section should find another section for integration with the target section in order to reconstruct a continuous and complete record.

4.2. Reconstructing the Paleoclimate of NE China

The MS curve of the loess–paleosol sequence reflects multi-cycle variations in the paleoclimate and can be compared with the marine oxygen isotope record [4,34,87]. Grain size is a good proxy for the Asian winter monsoon [6,30,88]. During dust transportation, wind sorting is an important factor in the abrasion and size reduction of dust particles [89]. In this study, the climate change information in NE China was interpreted based on the MS and content of the coarse fraction > 63 μm (Figure 7). The perpendicular direction

of the coarse fraction content > 63 μm represents the direction of dust transport, which corresponds to that of regional wind [90].

According to the marine isotope stage (MIS) boundary, the MIS 1/2, MIS 2/3, MIS 3/4, MIS 4/5, and LR04 ages were 11.7, 29, 57, and 71 ka, respectively [91]. The climatic evolution of the last glacial period in the DJG section can be divided into three large zones and ten sub-zones (Figure 7). The paleoclimate of NE China was generally divided into stages I, II, and III (Table 5). The climate changed from warm and humid to cold and dry from 71 to 57 ka during stage I (equivalent to MIS 4), alternated between cold and warm temperatures from 57 to 29 ka in stage II (equivalent to MIS 3), and was overall cold and dry from 29 to 11.7 ka but warm from 18 to 11.7 ka in stage III (equivalent to MIS 2) (Figure 7 and Table 5). The substantial strengthening of the winter monsoon around 39, 52, 56, and 62 ka was almost synchronous with the occurrence of the Heinrich event [92].

Table 5. Climatic information obtained by comparing MS and fraction of grain size > 63 μm of the DJG section.

| Stage	Sub-Zones	MS [a]	>63 μm	Paleoclimate Interpretation
Stage I (L_{1-3})	I-a ($L_{1-3}S_1$)	Highest	Low	The winter monsoon was weakened, and the climate was warm and humid.
	I-b	Low	High	The winter monsoon was strengthened, and the climate entered a cold and dry period.
	I-c	Minimum	Highest	The winter monsoon was strengthened, and the climate gradually turned colder and drier.
	I-d	Increased slowly	High	The winter monsoon prevailed, and the climate was cold.
Stage II (L_{1-2})	II-a	Had two peaks	Decreased gradually from 60% to 40%	The winter monsoon began to gradually weaken.
	II-b	Had two peaks and one valley	Decreased gradually from 40% to 20%	The climate was volatile.
	II-c	Had one peak	Decreased gradually	The climate of 32~29 ka was cold and dry.
Stage III (L_{1-1})	III-a	Decreased gradually	Increased gradually	The climate gradually deteriorated and became colder and drier.
	III-b	The lowest	Increased	The climate was dry and cold, and the temperature decreased significantly.
	III-c	Small peak	Increased gradually	The overall climate was dry and cold.

[a] MS, magnetic susceptibility.

In MIS 4, the MS curve fluctuation trend of the DJG section showed that the climate changed from warm to cold, which coincided with the gradually increasing ice volume in the benthic $\delta^{18}O$ curve (Figure 7) [93]. In MIS 3 (i.e., 57–29 ka), the climate recorded in the DJG section was unstable and fluctuated significantly (alternating between warm and cold), which was consistent with the unstable climate recorded by the benthic $\delta^{18}O$ curve. In MIS 2 (i.e., 29–11.7 ka), the cooling–drying trends recorded in the DJG loess section were correlated with the increase in high-latitude ice volume. This is consistent with the hypothesis that cooling and ice volume expansion at high latitudes were the drivers of long-term stepwise aridification of the Asian interior [1,26,94] (Figure 7).

In this study, the Yuanbao (YB) section of the CLP was selected for comparison with the DJG section (Figure 7). Chen et al. [95] pointed out that the YB section—located at the northwestern edge of the CLP—was a representative eolian loess depositional section, with the Malan loess layer (i.e., layer L_1) containing nine pedogenic layers. The results indicated that the YB section recorded a high-resolution history of summer and winter monsoon climate variations over the last 75 ka, which showed a high degree of similarity with the warm interstadials recorded in ice cores from Greenland and the Antarctic. Variation in the MS curve of the DJG section coincided well with the MS curve of the YB section, indicating

that the fluctuations in paleoclimate were consistent (Figure 7). During MIS 2, both DJG and YB sections recorded a generally weak summer monsoon (low MS values), while the winter monsoon was quite strong and variable, which coincided with cold global temperatures. During MIS 3, in the DJG and YB sections, the MS curves showed a similar pattern of variation, and the main MS peaks could be easily correlated between the two sections. Chen et al. [95] showed that the summer monsoon was generally very strong and variable, while the winter monsoon was quite weak during 50–30 ka. However, upon detailed comparison, the paleoclimate information reflected by the DJG section was not a one-to-one correspondence with the YB section. The differences may be the result of regional climatic effects and a relatively high degree of variability in the depositional environment over short distances [96]. During MIS 4, the climate recorded in the DJG section changed from warm and humid to cold and dry. Chen et al. [95] indicated that the summer monsoon was generally weak and showed a small range of variation, but in addition, the winter monsoon was not strong and did not show a range of variation during 70–50 ka. There were some differences in the start and end times of the warm period, which might have been due to the different dating methods.

Variations in grain-size distribution coincide well with loess and pedogenic layers (Figure 7). The percentage of coarse fraction can indicate variability in the Asian winter monsoon [88]. Several times, the content of coarse fraction in the DJG and YB sections decreased significantly, which corresponded to warm periods in the benthic $\delta^{18}O$ curve (Figure 7). The grain-size distribution curves (>40 μm) from the YB section displayed a high-frequency, high-amplitude pattern, while the DJG section had relatively low amplitudes. Moreover, it is noteworthy that the grain-size distribution of the DJG section was overall coarser than the YB section, which might have been caused by topographic variation and by the distance to dust sources [96]. Overall, the paleoclimate record preserved by the DJG section was consistent with that preserved by the benthic $\delta^{18}O$ curve and the YB section, demonstrating that the chronology of the DJG section was valid and could be used for paleoclimate reconstruction in NE China.
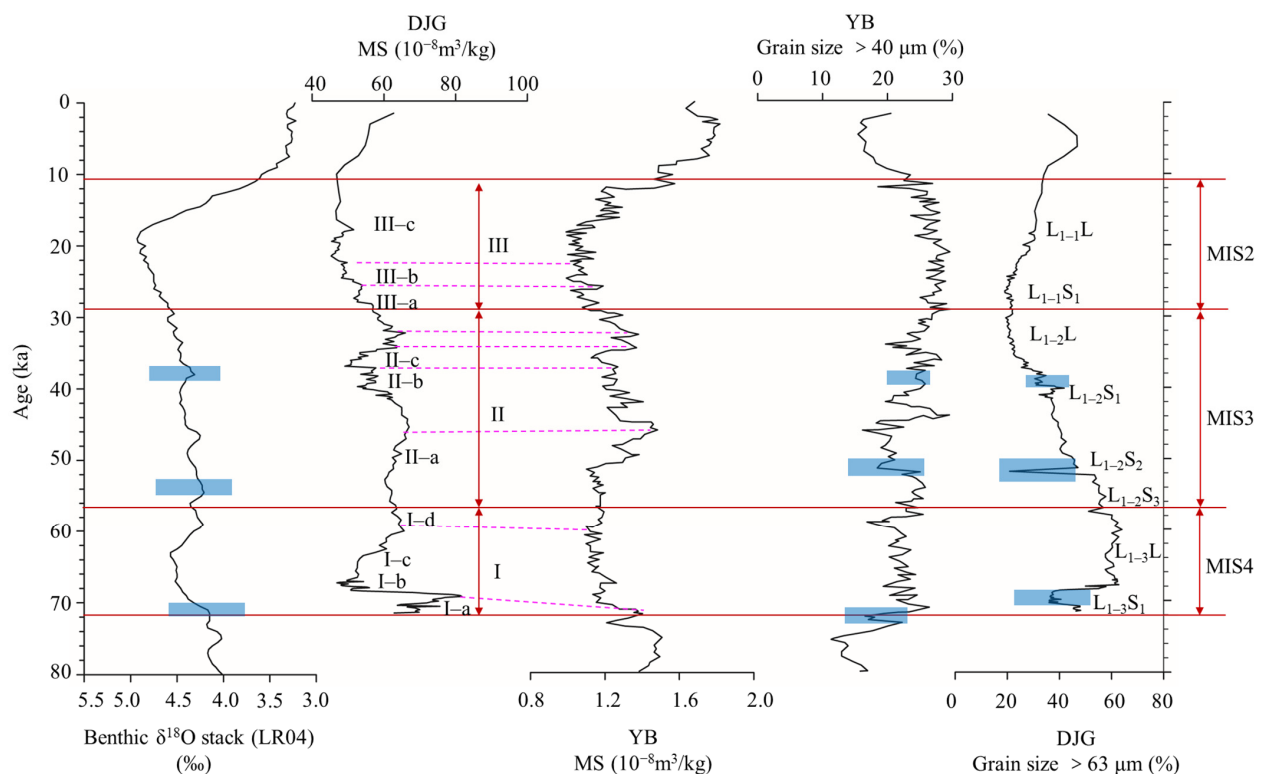
Figure 7. Comparisons of MS, fraction of grain size > 63 μm of the DJG section with the benthic $\delta^{18}O$ stack (LR 04) [93], and the YB section [95]. MS represents magnetic susceptibility; Md represents median

grain size; and the DJG and YB sections represent the Dajiugang and Yuanbao sections, respectively. The red lines represent the boundaries of the MIS stages. The pink dotted lines indicate MS peaks of the DJG section, corresponding to MS peaks of the YB section. The blue squares show the warm periods in the DJG and YB sections, which correspond to the benthic δ^{18}O stack.

5. Conclusions

This study showed that the DJG section could be merged with the upper part (layer L1) of the target SBH section. The DJG section was close in proximity to the SBH section, and the parent material and genesis of these two sections were similar, with clear and identical depositional ages. In particular, the DJG section recorded multiple climate cycles and could overcome the lack of paleoclimatic information in the SBH section from 71 ka. The paleoclimate record preserved by the DJG section was consistent with the benthic δ18O stack (LR 04) and the YB section. The overall climate of NE China during 29–11.7, 57–29, and 71–57 ka was cold and dry, alternately cold and warm, and warm and wet to cold and dry, respectively. The paleoclimate information of the target SBH section during 84–71 ka will need to be integrated with another loess section because the DJG section was discontinuous during 181–71 ka. Integrating the target sections could be an alternative method of reconstructing long-term continuous paleoclimate records.

References

1. Ding, Z.L.; Derbyshire, E.; Yang, S.L.; Yu, Z.W.; Xiong, S.F.; Liu, T.S. Stacked 2.6-Ma grain size record from the Chinese loess based on five sections and correlation with the deep-sea δ^{18}O record. *Paleoceanography* **2002**, *17*, 5–21. [CrossRef]
2. Obreht, I.; Zeeden, C.; Hambach, U.; Veres, D.; Marković, S.B.; Bösken, J.; Bačević, N.; Gavrilov, M.B.; Lehmkuhl, F. Tracing the influence of Mediterranean climate on Southeastern Europe during the past 350,000 years. *Sci. Rep.* **2016**, *6*, 36334. [CrossRef]
3. Liu, T.S.; Ding, Z.L. Chinese loess and the paleomonsoon. *Annu. Rev. Earth Planet* **1998**, *26*, 111–145. [CrossRef]
4. An, Z.S.; Kukla, G.J.; Porter, S.C.; Xiao, J.L. Magnetic susceptibility evidence of monsoon variation on the Loess Plateau of central China during the last 130,000 years. *Quat. Res.* **1991**, *36*, 29–36. [CrossRef]
5. Anwar, T.; Kravchinsky, V.A.; Zhang, R.; Koukhar, L.P.; Yang, L.; Yue, L. Holocene climatic evolution at the Chinese Loess Plateau: Testing sensitivity to the global warming-cooling events. *J. Asian Earth Sci.* **2018**, *166*, 223–232. [CrossRef]
6. Guo, F.; Clemens, S.C.; Wang, T.; Wang, Y.; Liu, Y.; Wu, F.; Liu, X.; Jin, Z.; Sun, Y. Monsoon variations inferred from high-resolution geochemical records of the Linxia loess/paleosol sequence, western Chinese Loess Plateau. *Catena* **2021**, *198*, 2–11. [CrossRef]
7. Buggle, B.; Hambach, U.; Glaser, B.; Gerasimenko, N.; Marković, S.; Glaser, I.; Zöller, L. Stratigraphy, and spatial and temporal paleoclimatic trends in Southeastern/Eastern European loess–paleosol sequences. *Quat. Int.* **2009**, *196*, 86–106. [CrossRef]
8. Haase, D.; Fink, J.; Haase, G.; Ruske, R.; Pécsi, M.; Richter, H.; Altermann, M.; Jäger, K.D. Loess in Europe—Its spatial distribution based on a European Loess Map, scale 1:2,500,000. *Quat. Sci. Rev.* **2007**, *26*, 1301–1312. [CrossRef]
9. Panin, P.G.; Filippova, K.G.; Bukhonov, A.V.; karpukhina, N.V.; Ruchkin, M.V. High-resolution analysis of the Likhvin loess-paleosol sequence (the central part of the East European plain, Russia). *Catena* **2021**, *205*, 105445. [CrossRef]
10. Velichko, A.A. Loess-paleosol formation on the Russian plain. *Quat. Int.* **1990**, *7/8*, 103–114. [CrossRef]
11. Hall, R.D.; Anderson, A.K. Comparative soil development of Quaternary paleosols of the central United States. *Palaeogeogr. Palaeoclimatol. Palaeoecol.* **2000**, *158*, 109–145. [CrossRef]
12. Plata, J.M.; Rodríguez, R.; Preusser, F.; Boixadera, J.; Balash, J.C.; Antúnez, M.; Poch, R.M. Red soils in loess deposits of the Eastern Ebro Valley. *Catena* **2021**, *204*, 105430. [CrossRef]

13. Heller, F.; Liu, T.S. Palaeoclimatic and sedimentary history from magnetic susceptibility of loess in China. *Geophys. Res. Lett.* **1986**, *13*, 1169–1172. [CrossRef]

14. Sun, Z.X.; Jiang, Y.Y.; Wang, Q.B.; Owens, P.R. Geochemical characterization of the loess-paleosol sequence in northeast China. *Geoderma* **2018**, *321*, 127–140. [CrossRef]

15. Gebrechorkos, S.H.; Hülsmann, S.; Bernhofer, C. Statistically downscaled climate dataset for East Africa. *Sci. Data* **2019**, *6*, 31. [CrossRef]

16. Xie, S.P.; Vecchi, G.A.; Collins, M.; Delworth, T.L.; Hall, A.; Hawkins, E.; Johnson, N.C.; Cassou, C.; Giannini, A.; Watanabe, M. Towards predictive understanding of regional climate change. *Nat. Clim. Change* **2015**, *5*, 921–930. [CrossRef]

17. Sun, Y.B.; Wang, X.L.; Liu, Q.S.; Clemens, S.C. Impacts of post-depositional processes on rapid monsoon signals recorded by the last glacial loess deposits of northern China. *Earth Planet. Sci. Lett.* **2010**, *289*, 171–179. [CrossRef]

18. Dodonov, A.E.; Zhou, L.P. Loess deposition in Asia: Its initiation and development before and during the Quaternary. *Episodes* **2008**, *31*, 222–225. [CrossRef]

19. Li, Y.; He, S.; Peng, J.; Xu, Q.; Aydin, A.; Xu, Y. Loess geology and surface processes: An introductory note. *J. Asian Earth Sci.* **2020**, *200*, 104477. [CrossRef]

20. Liu, T.S. *Loess and Environment*; Science Press: Beijing, China, 1985. (In Chinese)

21. Chen, Y.M.; Gong, H.L. *Study on Loess Records of Climatic Instability during Last Glacial Period*; China Environmental Science Press: Beijing, China, 2007. (In Chinese)

22. Hu, X.F.; Wei, J.; Du, Y.; Xu, L.F.; Wang, H.B.; Zhang, G.L.; Wei, Y.; Zhu, L.D. Regional distribution of the Quaternary red clay with aeolian dust characteristics in subtropical China and its paleoclimatic implications. *Geoderma* **2010**, *159*, 317–334. [CrossRef]

23. Liang, L.J.; Sun, Y.B.; Beets, C.J.; Prins, M.A.; Wu, F.; Vandenberghe, J. Impacts of grain size sorting and chemical weathering on the geochemistry of Jingyuan loess in the northwestern Chinese Loess Plateau. *J. Asian Earth Sci.* **2013**, *69*, 177–184. [CrossRef]

24. Liu, T.S. *Loess Accumulation in China*; Science Press: Beijing, China, 1965. (In Chinese)

25. Zeng, L.; Lu, H.Y.; Yi, S.W.; Xu, Z.W.; Qiu, Z.M.; Yang, Z.Y.; Li, Y.X. Magnetostratigraphy of loess in northeastern China and paleoclimatic changes. *Sci. China Press* **2011**, *56*, 2267–2275. (In Chinese)

26. Zeng, L.; Lu, H.Y.; Yi, S.W.; Stevens, T.; Xu, Z.W.; Zhuo, H.X.; Yu, K.F.; Zhang, H.Z. Long-term Pleistocene aridification and possible linkage to high-latitude forcing: New evidence from grain size and magnetic susceptibility proxies from loess-paleosol record in northeastern China. *Catena* **2017**, *154*, 21–32. [CrossRef]

27. Zeng, L.; Lu, H.Y.; Yi, S.W.; Li, Y.X.; Lv, A.Q.; Zhang, W.C.; Xu, Z.W.; Wu, H.F.; Feng, H.; Cui, M.C. New magnetostratigraphic and pedostratigraphic investigations of loess deposits in north-east China and their implications for regional environmental change during the Mid-Pleistocene climatic transition. *J. Quat. Sci.* **2016**, *31*, 20–32. [CrossRef]

28. Yi, S.W.; Buylaert, J.P.; Murray, A.S.; Thiel, C.; Zeng, L.; Lu, H.Y. High resolution OSL and post-IR IRSL dating of the last interglacial-glacial cycle at the Sanbahuo loess site (northeastern China). *Quat. Geochronol.* **2015**, *30*, 200–206. [CrossRef]

29. An, Z.S. The history and variability of the East Asian paleomonsoon climate. *Quat. Sci. Rev.* **2000**, *19*, 171–187. [CrossRef]

30. Lu, H.Y.; An, Z.S. Paleoclimatic significance of grain size of loess-palaeosol deposit in Chinese Loess Plateau. *Sci. China Ser. D* **1998**, *41*, 626–631. [CrossRef]

31. Zhang, Q.; Xu, P.; Qian, H.; Hou, K. Response of grain-size components of loess-paleosol sequence to Quaternary climate in the Southern Loess Plateau, China. *Arab. J. Geosci.* **2020**, *13*, 815. [CrossRef]

32. Evans, M.E.; Heller, F. Magnetism of loess/palaeosol sequences: Recent developments. *Earth-Sci. Rev.* **2001**, *54*, 129–144. [CrossRef]

33. Sun, W.W.; Banerjee, S.K.; Hunt, C.P. The role of maghemite in the enhancement of magnetic signal in the Chinese loess-paleosol sequence: An extensive rock magnetic study combined with citrate-bicarbonate-dithionite treatment. *Earth Planet. Sci. Lett.* **1995**, *133*, 493–505. [CrossRef]

34. Liu, Q.; Jin, C.; Hu, P.; Jiang, Z.; Ge, K.; Roberts, A.P. Magnetostratigraphy of Chinese loess–paleosol sequences. *Earth-Sci. Rev.* **2015**, *150*, 139–167. [CrossRef]

35. Nie, J.S.; King, J.W.; Fang, X.M. Link between benthic oxygen isotopes and magnetic susceptibility in the red-clay sequence on the Chinese Loess Plateau. *Geophys. Res. Lett.* **2008**, *35*, L03703. [CrossRef]

36. Stockmann, U.; Minasny, B.; Mcbratney, A.B. Advances in agronomy quantifying processes of pedogenesis. *Adv. Agron.* **2011**, *113*, 1–74.

37. Sun, Z.X.; Owens, P.R.; Han, C.L.; Chen, H.; Wang, X.L.; Wang, Q.B. A quantitative reconstruction of a loess–paleosol sequence focused on paleosol genesis: An example from a section at Chaoyang, China. *Geoderma* **2016**, *266*, 25–39. [CrossRef]

38. Huggett, R.J. Soil chronosequences, soil development, and soil evolution: A critical review. *Catena* **1998**, *32*, 155–172. [CrossRef]

39. Jiang, Y.Y.; Sun, Z.X.; Wang, Q.B.; Sun, Z.G.; Jiang, Z.D.; Gu, H.Y.; Libohova, Z.; Owens, P.R. Characteristics of the typical loess profile with a macroscopic tephra layer in the northeast China and the paleoclimatic significance. *Catena* **2021**, *198*, 105043. [CrossRef]

40. Liaoning Geological Team. *Liaoning Quaternary*; Geological Press: Reston, VA, USA, 1983. (In Chinese)

41. Lv, A.Q.; Lu, H.Y.; Zeng, L.; Yi, S.W.; Zhuo, H.X.; Xu, Z.W.; Zhang, W.C. Evolution of Horqin and Otindag dune fields since 1.08 Ma recorded by grain size of loess in Chifeng, northeastern China. *J. Desert Res.* **2017**, *37*, 659–665. (In Chinese)

42. Schoeneberger, P.J.; Wysocki, D.A.; Benham, E.C. Soil-Survey-Staff, 2012. In *Field Book for Describing and Sampling Soils*; Version 3.0; Natural Soil Survey Center: Lincoln, NE, USA, 2012.

43. Birkeland, P.W. Soil-geomorphic research—A selective overview. *Geomorphology* **1990**, *3*, 207–224. [CrossRef]
44. Buol, S.W.; Southard, R.J.; Graham, R.C.; Mcdaniel, P.A. Soil genesis and classification. *Q. Rev. Biol.* **2011**, *18*, 609.
45. Nettleton, W.D.; Olson, C.G.; Wysocki, D.A. Paleosol classification: Problems and solutions. *Catena* **2000**, *41*, 61–92. [CrossRef]
46. Akselrod, M.S.; Bøtter-Jensen, L.; Mckeever, S.W.S. Optically stimulated luminescence and its use in medical dosimetry. *Radiat. Meas.* **2006**, *41*, S78–S99. [CrossRef]
47. Thompson, R.; Oldfield, F. *Environmental Magnetism*; Allen and Unwin: Crows Nest, Australia, 1986.
48. Gee, G.W.; Or, D. Particle size analysis. In *Methods of Soil Analysis, Part 4 Physical Methods*; Dane, J.H., Topp, C., Eds.; Soil Science Society of America: Madison, WI, USA, 2002; pp. 255–293.
49. Zhang, G.L.; Gong, Z.T. *Soil Survey Laboratory Methods*; China Science Press: Beijing, China, 2012. (In Chinese)
50. Thomas, A.; Filippov, L.O. Fractures, fractals and breakage energy of mineral particles. *Int. J. Miner. Process.* **1999**, *57*, 285–301. [CrossRef]
51. Grossman, R.B.; Reinsch, T.G. The solid phase, 2.1 bulk density and linear extensibility. In *Methods of Soil Analysis, Part 4—Physical Methods*; Soil Science Society of America Book Series; Soil Science Society of America: Madison, WI, USA, 2002; pp. 229–240.
52. Ren, S.F.; Zheng, X.M.; Ai, D.S.; Zhou, L.M.; Wang, X.Y.; Shen, M.N.; Chen, S.J. The Improvement of carbonate content of the Xiashu Loess by measuring gas volume method. *Res. Explor. Lab.* **2014**, *33*, 8–12. (In Chinese)
53. Górecka, H.; Chojnacka, K.; Górecki, H. The application of ICP-MS and ICP-OES in determination of micronutrients in wood ashes used as soil conditioners. *Talanta* **2006**, *70*, 950–956. [CrossRef]
54. Lu, Y.C.; Wang, X.L.; Wintle, A.G. A new OSL chronology for dust accumulation in the last 130,000 yr for the Chinese Loess Plateau. *Quat. Res.* **2007**, *67*, 152–160. [CrossRef]
55. Roberts, R.M. Assessing the effectiveness of the double-SAR protocol in isolating a luminescence signal dominated by quartz. *Radiat. Meas.* **2007**, *42*, 1627–1636. [CrossRef]
56. Lai, Z.P.; Brückner, H. Effects of feldspar contamination on equivalent dose and the shape of growth curve for OSL of silt-sized quartz extracted from Chinese loess. *Geochronometria* **2008**, *30*, 49–53. [CrossRef]
57. Buylaert, J.P.; Murray, A.S.; Vandenberghe, D.; Vriend, M.; De Corte, F.; Vandenhaute, P. Optical dating of Chinese loess using sand-sized quartz: Establishing a time frame for late Pleistocene climate changes in the western part of the Chinese loess plateau. *Quat. Geochronol.* **2008**, *3*, 99–113. [CrossRef]
58. Mahan, S.A.; Rittenour, T.M.; Nelson, M.S.; Ataee, N.; Brown, N.; DeWitt, R.; Durcan, J.; Evans, M.; Feathers, J.; Frouin, M.; et al. *Guide for Interpreting and Reporting Luminescence Dating Results*; Geological Society of America Bulletin: Boulder, CO, USA, 2022.
59. Bøtter-Jensen, L.; Thomsen, K.J.; Jain, M. Review of optically stimulated luminescence (OSL) instrumental developments for retrospective dosimetry. *Radiat. Meas.* **2010**, *45*, 253–257. [CrossRef]
60. Murray, A.S.; Wintle, A.G. Luminescence dating of quartz using an improved single-aliquot regenerative-dose protocol. *Radiat. Meas.* **2000**, *32*, 57–73. [CrossRef]
61. Aitken, M.J. *An Introduction to Optical Dating*; Oxford University Press: London, UK, 1998; pp. 39–44.
62. Cremeens, D.L.; Mokma, D.L. Argillic horizon expression and classification in the soils of two michigan hydrosequences. *Soil Sci. Soc. Am. J.* **1986**, *50*, 1002–1007. [CrossRef]
63. Kukla, G.; Heller, F. Pleistocene climate in China dated by magnetic susceptibility. *Geology* **1988**, *16*, 811–814. [CrossRef]
64. Torrent, J.; Schwertmann, U.; Fechter, H.; Alferez, F. Quantitative relationships between soil color and hematite content. *Soil Sci.* **1983**, *136*, 354–358. [CrossRef]
65. Huang, C.M.; Gong, Z.T. Progress in quantitative research on soil genesis and development. *Soil Sci.* **2000**, *3*, 145–166. (In Chinese)
66. Lucke, B.; Sprafke, T. Correlation of soil color, redness ratings, and weathering indices of Terrae Calcis along a precipitation gradient in northern Jordan. *Erlanger Geogr. Arb. Band* **2015**, *42*, 53–68.
67. Buggle, B.; Glaser, B.; Hambach, U.; Gerasimenko, N.; Markovi, S. An evaluation of geochemical weathering indices in loess–paleosol studies. *Quat. Int.* **2011**, *240*, 12–21. [CrossRef]
68. Drees, L.R.; Wilding, L.P. Elemental Variability Within a Sampling Unit1. *Soil Sci. Soc. Am. J.* **1973**, *37*, 82–87. [CrossRef]
69. Gallet, S.; Jahn, B.M.; Torii, M. Geochemical characterization of the Luochuan loess-paleosol sequence, China, and paleoclimatic implications. *Chem. Geol.* **1996**, *133*, 67–88. [CrossRef]
70. Marsan, F.A.; Bain, D.C.; Duthie, D.M.L. Parent material uniformity and degree of weathering in a soil chronosequence, northwestern Italy. *Catena* **1988**, *15*, 507–517. [CrossRef]
71. Chen, L.M. *Pedogenesis of a Typical Stagnic Anthrosols Chronosequence*; Chinese Academy of Sciences: Beijing, China, 2009. (In Chinese)
72. Chapman, S.L.; Horn, M.E. Parent material uniformity and origin of silty soils in Northwest Arkansas based on Zirconium-Titanium contents. *Soil Sci. Soc. Am. J.* **1968**, *32*, 265–271. [CrossRef]
73. Sun, D.H.; Bloemendal, J.; Rea, D.K.; Vandenberghe, J.; Jiang, F.C.; An, Z.S.; Su, R.X. Grain-size distribution function of polymodal sediments in hydraulic and aeolian environments, and numerical partitioning of the sedimentary components. *Sediment. Geol.* **2002**, *152*, 263–277. [CrossRef]
74. Pye, K. *Aeolian Dust and Dust Deposits*; Academic Press: San Diego, CA, USA, 1987; pp. 1–334.
75. Sun, Z.X.; Jiang, Y.Y.; Wang, Q.B.; Owens, P.R. A fractal evaluation of particle size distributions in an eolian loess-paleosol sequence and the linkage with pedogenesis. *Catena* **2018**, *165*, 80–91. [CrossRef]

76. Lu, H.Y.; An, Z.S. Comparison of grain-size distribution of red clay and loess-paleosol deposits in Chinese Loess Plateau. *Acta Sedimentol. Sin.* **1999**, *17*, 226–232. (In Chinese)
77. Verosub, K.L.; Fine, P.; Singer, M.J.; Tenpas, J. Pedogenesis and paleoclimate: Interpretation of the magnetic susceptibility record of Chinese loess-paleosol sequences. *Geology* **1993**, *21*, 1011–1014. [CrossRef]
78. An, Z.S.; Liu, T.S.; Lu, Y.C.; Porter, S.C.; Kukla, G.J.; Wu, X.H.; Hua, Y.M. The long-term paleomonsoon variation recorded by the loess-paleosol sequence in central China. *Quat. Int.* **1990**, *7–8*, 91–95.
79. Eze, P.N.; Molwalefhe, L.N.; Kebonye, N.M. Geochemistry of soils of a deep pedon in the Okavango Delta, NW Botswana: Implications for pedogenesis in semi-arid regions. *Geoderma Reg.* **2020**, *24*, e00352. [CrossRef]
80. Fedo, C.M.; Nesbitt, H.W.; Young, G.M. Unraveling the effects of potassium metasomatism in sedimentary rocks and paleosols, with implications for paleoweathering conditions and provenance. *Geology* **1995**, *23*, 921–924. [CrossRef]
81. Chen, J.; An, Z.S.; Head, J. Variation of Rb/Sr Ratios in the loess-paleosol Sequences of central China during the last 130,000 Years and their Implications for monsoon paleoclimatology. *Quat. Res.* **1999**, *51*, 215–219. [CrossRef]
82. Li, X.Y. *High-Resolution Geochemical Studies of the Holocene Loess-Paleosol Profile in the Upper-Reaches of the Huaihe River*; Shanxi Normal University: Xi'an, China, 2007. (In Chinese)
83. Sümegi, P.; Gulyás, S.; Molnár, D.; Sümegi, B.P.; Almond, P.C.; Vandenberghe, J.; Zhou, L.; Pál-Molnár, E.; Törőcsik, T.; Hao, Q.; et al. New chronology of the best developed loess/paleosol sequence of Hungary capturing the past 1.1 ma: Implications for correlation and proposed pan-Eurasian stratigraphic schemes. *Quat. Sci. Rev.* **2018**, *191*, 144–166. [CrossRef]
84. Wang, H.B.; Chen, F.H.; Zhang, J.W. Environmental significance of grain size of loess-paleosol sequence in western part of Chinese loess plateau. *J. Desert Res.* **2002**, *22*, 21–26. (In Chinese)
85. Lu, L.Z.; Shi, Z.T. Analysis of sediment grain size parameter connotation and calculation method. *Environ. Sci. Manag.* **2010**, *35*, 54–60. (In Chinese)
86. Qiao, Y.S.; Guo, Z.T.; Hao, Q.Z.; Yin, Q.Z.; Yuan, B.Y.; Liu, T.S. The grain size characteristics of the loess-paleosol sequence in miocene and its indicative significance to its genesis. *Sci. China Ser. D Earth Sci.* **2006**, *36*, 646–653. (In Chinese)
87. Feng, Z.D.; Chen, F.H. Problems of the magnetic susceptibility signature as the proxy of the summer monsoon intensity in the Chinese Loess Plateau. *Chin. Sci. Bull.* **1999**, *S1*, 106–113.
88. Sun, D.H. Monsoon and westerly circulation changes recorded in the late Cenozoic aeolian sequences of Northern China. *Glob. Planet. Change* **2004**, *41*, 63–80.
89. Sun, J.M. Provenance of loess material and formation of loess deposits on the Chinese Loess Plateau. *Earth Planet. Sci. Lett.* **2002**, *203*, 845–859. [CrossRef]
90. Pye, K. The nature, origin and accumulation of loess. *Quat. Sci. Rev.* **1995**, *14*, 653–667. [CrossRef]
91. Lisiecki, L.E.; Raymo, M.E. Diachronous benthic δ^{18}O responses during late Pleistocene terminations. *Paleoceanography* **2009**, *24*, PA3210. [CrossRef]
92. Porter, S.C.; An, Z.S. Correlation between climate events in the North Atlantic and China during the last glaciation. *Nature* **1995**, *375*, 305–308. [CrossRef]
93. Lisiecki, L.E.; Raymo, M.E. A Pliocene-Pleistocene stack of 57 globally distributed benthic δ^{18}O records. *Paleoceanography* **2005**, *20*, PA1003.
94. Fan, Y.J.; Jia, J.; Liu, Y.; Zhao, L.; Liu, X.; Gao, F.Y.; Xia, D.S. Millennial-scale climate oscillations over the last two climatic cycles revealed by a loess–paleosol sequence from central Asia. *J. Asian Earth Sci.* **2022**, *240*, 105435. [CrossRef]
95. Chen, F.H.; Bloemendal, J.; Wang, J.M.; Li, J.J.; Oldfield, F. High-resolution multi-proxy climate records from Chinese loess: Evidence for rapid climatic changes over the last 75 kyr. *Palaeogeogr. Palaeoclimatol. Palaeoecol.* **1997**, *130*, 323–335. [CrossRef]
96. Lu, H.; Wang, X.; Li, L. Aeolian sediment evidence that global cooling has driven late Cenozoic stepwise aridification in central Asia. *Geol. Soc. Lond. Spec. Publ.* **2010**, *342*, 29–44. [CrossRef]